W. J. DERNER
R. A. GOODELLE
L. E. ROOT
Rollway Bearing Co., Inc.,
Liverpool, N. Y.
R. RUNG
Applied Technology Associates,
Ramsey, N. J.

# The Hollow-Ended Roller[1]—A Solution for Improving Fatigue Life in Asymmetrically Loaded Cylindrical Roller Bearings

*To reduce the influence of misalignment (asymmetrical loading) on cylindrical roller bearings it is necessary to supplement the crown modifications of bearing elements. A unique hollow-ended roller design was developed for this purpose employing a three-dimensional finite element elasticity study to determine the stress state in the flexible rim section. The results when combined with the classical Hertzian contact stress distribution result in an accurate description of the shear stress field throughout the roller rim sections. Results of fatigue tests run under asymmetrically distributed loads supported the analytical efforts demonstrating significant improvements in $L_{10}$ lives for the hollow-ended roller as compared to a solid roller. Peak stresses occurred in the vicinity of the contact area for both types of rollers with the solid exhibiting stresses 5 percent or more higher than those found in the hollow-ended type. Of equal importance, the observed failure mode for hollow-ended rollers under heavy load fatigue test conditions is one of conventional subsurface initiated O.D. spalling, thereby proving the rim design to be structurally sound.*

## Introduction

In applications of cylindrical roller bearings subjected to heavy loads and significant deflections, misalignment has been found to drastically shorten life [1].[2] Specially developed crowning may alleviate this problem somewhat but such modification of bearing elements must be supplemented if significant improvements in bearing life are to be achieved. To this end, development of hollow-ended cylindrical rollers was initiated with the objective of increasing the range of misalignment which a bearing could endure while also increasing reliability and life. It was felt that this could best be achieved by improving load distribution.

Both analytical and experimental studies were conducted in developing a rigorous stress analysis technique from which design criteria could be determined. These analyses were substantiated by fatigue tests designed to reveal the failure mode and its origin and to compare the fatigue lives of hollow-ended rollers with respect to the conventional crowned solid type. Of basic importance was (*a*) a thorough understanding of the complex stress distribution throughout the entire rim, (*b*) the relation of the stress distribution to the shape of the bore in the roller ends, (*c*) the relative dimensions of the roller, and (*d*) an exact description of the loading imposed on the bearing.

Computer solutions were obtained for the stress distribution throughout the roller using a three-dimensional finite element analysis. The success of applying this method to this particular problem requires an accurate description of the load distribution imposed on the roll body. The authors' footprint technique [2 and 3] was used to determine the distribution of the applied load on the roller that existed in the actual fatigue test rig. This method involves chemically etching a steel plate or race resulting in a thin carbon film remaining on the surface. Rollers are statically loaded on the unlubricated surface yielding a permanent record of the elastic contact area upon load release. The measured (observed) widths ($2b$) of the footprint must be modified to exclude the influence of the etch film thickness. Once corrected, this adjusted contact area (apparent area) may be constructed graphically and represents the elastic contact area that would have existed in reality had there been no etch film present. Dividing the area into numerous increments allows equivalent width dimensions (based on rectangular increments) to be determined for each increment, yielding the unit loading at these respective points [2].

[1] Patent applied for.

[2] Numbers in brackets designate References at end of paper.

Contributed by the Lubrication Division of The American Society of Mechanical Engineers and presented at the ASLE-ASME Joint Lubrication Conference, Pittsburgh, Pa., October 5–7, 1971. Manuscript received by the Lubrication Division March 28, 1971; revised manuscript received July 6, 1971. Paper No. 71-Lub-14.

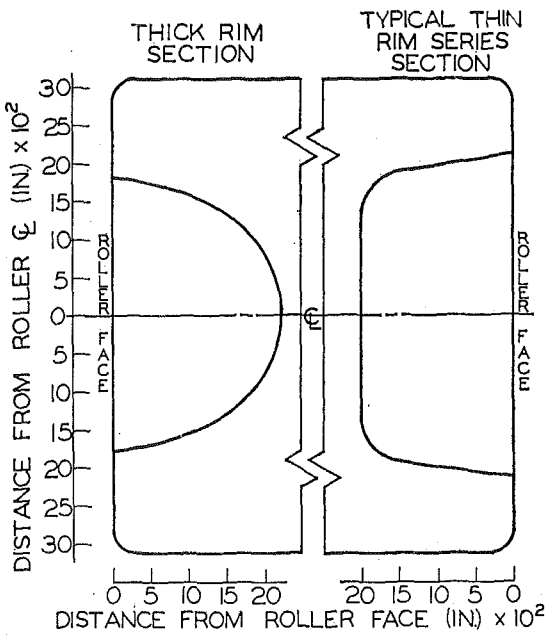


**Fig. 1 Thick rim and thin rim series hollow-ended roller (0.625 × 0.625 in.) comparative bore geometry**

All testing and comparisons were made on a basic roller 0.625 in. long × 0.625 in. dia, made of case hardened 8620 steel. Preliminary investigations, which included analytical and fatigue test efforts, eliminated several bore shapes and rim thicknesses. Fatigue failure was found to be highly dependent on the geometry of the bore. Under high operating loads and misalignment, the comparatively thin-rimmed series of hollow-ended rollers, Fig. 1, would crack in the bore of the rim rapidly generating into an O.D. spall (this series of hollow-ended rollers still had a longer fatigue life than the solid rollers under similar operating conditions as displayed later).

Having thus found a satisfactory bore shape (denoted thick-rim in Fig. 1) with sound rim structure, the following evaluation of this roller can be made with respect to the conventional solid configuration.

## Finite Element Method

A computer program was developed, based upon a finite element, direct stiffness method, to determine the three-dimensional stress state existing in the hollow-ended roller subjected to a line load. This is an accepted technique for handling complex stress problems and widely used as a method for solving structural problems [4]. The finite element method has recently been extended to include problems of the elastic continuum. This method is a proper selection in this case as it inherently provides complete generality with regard to geometry and field property variations while no difficulty is encountered in prescribing

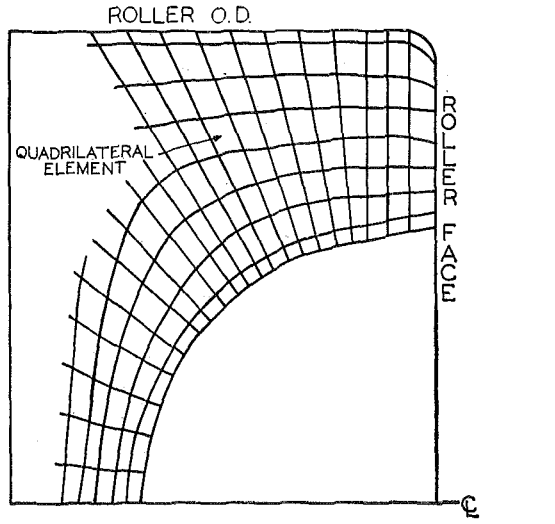


**Fig. 2 Finite element idealization for rim section of hollow-ended roller**

boundary, symmetry and loading conditions. A two-dimensional analysis is extended into three-dimensional analysis (presented as a short discussion in the appendix for the interested reader) which permits analyzing bodies of revolution subjected to loads expressed as any function of $R$, $Z$, and the Fourier series in $\theta$. The convergence of solution and the adequacy of the finite element mesh was investigated considering two mathematical models of the same roller configuration. The model with smaller element sizes when subjected to various Fourier harmonic load coefficients proved to change the solution by only 1 percent over the larger which incorporated fewer finite elements. The final finite element idealization (grid development) selected is displayed in Fig. 2. This grid is made up of many quadrilateral elements each consisting of four triangles (not shown). The stress results are read out at the centroids of the quadrilaterals and are obtained from sophisticated averaging of the stress in the triangular elements.

## Numerical Stress Analysis

Analytical treatment of this problem provides a numerical solution for the stresses induced in a conical shell elastically supported at one end and under the influence of an asymmetrical self-equilibrating line load.

The load distribution, Fig. 3, was obtained empirically from static footprint tests of actual hollow-ended, cylindrical rollers loaded between misaligned planes. The loading, not being symmetric about the mid-plane, is therefore separated into symmetric and antisymmetric components about the plane. The line loads are applied at the planes $\theta = 0$ deg and $\theta = 180$ deg, with the resulting normal pressure distribution symmetric about these planes ($\theta = 0$ deg plane shown in Fig. 4). To determine the stress state in the roller, but neglecting for the moment the local

## Nomenclature

$b$ = contact area half-width, in.
$l_{EFF}$ = effective length (actual), in.
$l$ = incremental length, in.
$L_{10}$ = bearing life rating (AFBMA)
$m$ = any integer
$P$ = incremental load, lb
$p$ = normal Hertzian pressure, psi
$P/l$ = unit load, lb/in.
$U$ = amplitude of the displacement, in.
$u$ = displacement at any point, in.
$\sigma$ = principal stress, psi
$\sigma^*$ = approximate stress, psi
$\hat{\sigma}$ = accurate stress, psi
$\tau$ = shear stress, psi
$I$ = denotes stress plane
$J$ = denotes stress plane

*Subscripts*

$H$ = denotes hollow-ended roller
$R$ = denotes radial direction
$n$ = denotes direction normal to bore surface
$S$ = denotes solid roller
$t$ = denotes tangential direction at bore surface
$Z$ = denotes axial direction
$\theta$ = denotes circumferential direction
0 = denotes maximum

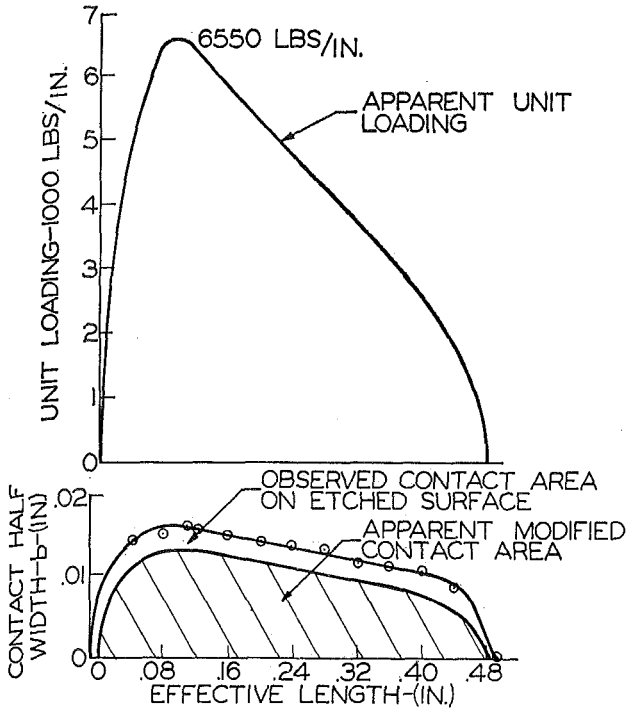


Fig. 3 Load distribution determined from analysis of contact area (footprint) for hollow-ended roller

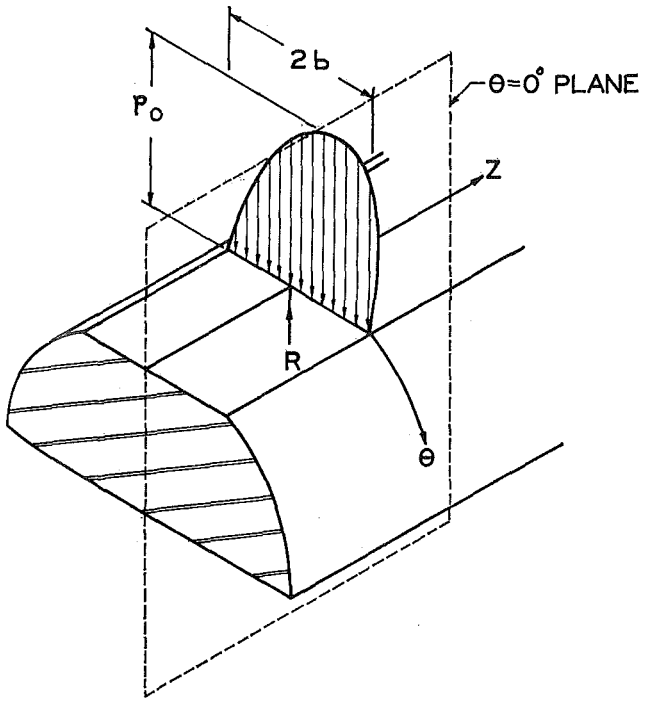


Fig. 4 Roller coordinate system

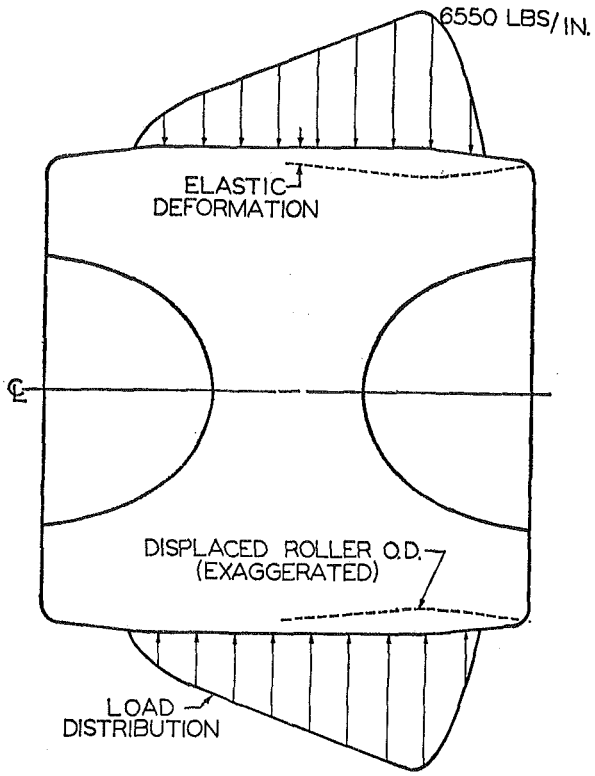


Fig. 5 Elastic radial displacement of hollow-ended roller rim at contact surface

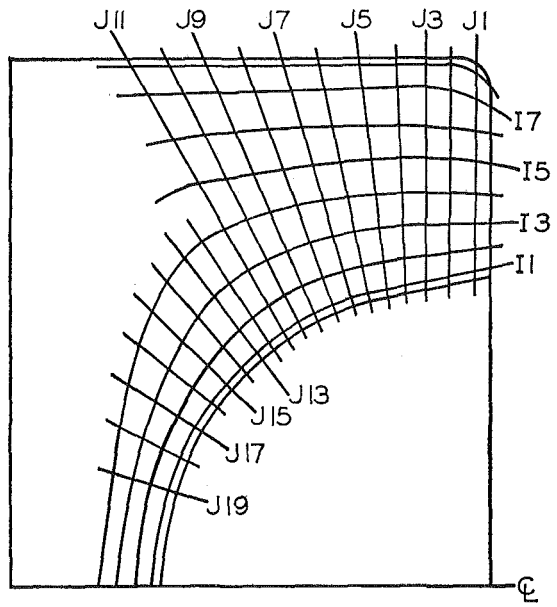


Fig. 6 Stress planes (I and J) with stresses ($\sigma_H$*) computed at intersections

Hertzian contact stress state, the parabolic distribution of pressure is replaced by a concentrated line load whose intensity varies along the $Z$ axis. This line load is considered to conform to a cosine series represented by an expansion in the Fourier series. The load distribution data, Fig. 3, is used to determine the Fourier coefficients which forms input data for the computer analysis or:

$$p = \frac{P/l}{\pi r} + \sum_{m=2,\,4}^{12} \frac{2P/l}{\pi r} \cos m\theta$$

It was necessary to utilize $m = 12$ for sufficient accuracy (theoretically $m = \infty$). As the hollow-ended roller is symmetric about its mid-plane, and as the maximum stresses will occur in the rim section under the maximum loading, the use of only a quarter-section is permitted in the finite element idealization (viz. grid development; see Fig. 2).

The elastic displacement of the rim is shown schematically in Fig. 5. Inspection shows that the rim does not deflect in the same classical manner, for example, as a conventional cantilever beam subjected to a distributed load; rather, the rim has a maximum deflection associated with the peak unit load.

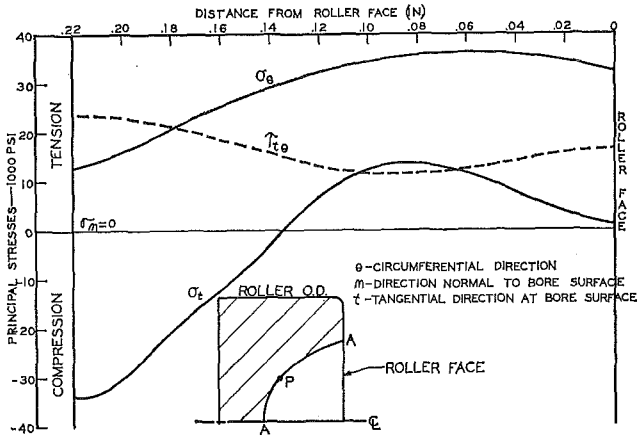


**Fig. 7 Principal stresses and maximum shear along the bore at $I = 1$ in plane of load ($\theta = 0$ deg)**

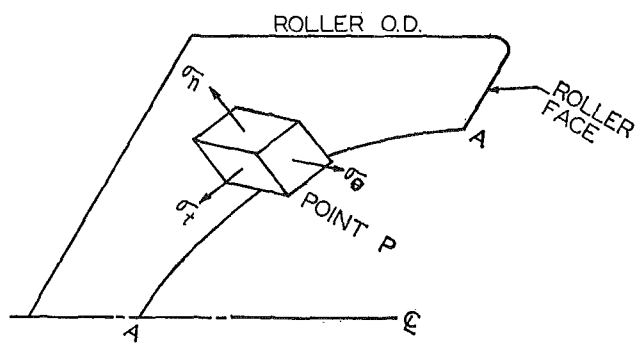


**Fig. 8 Bore stress orientation**

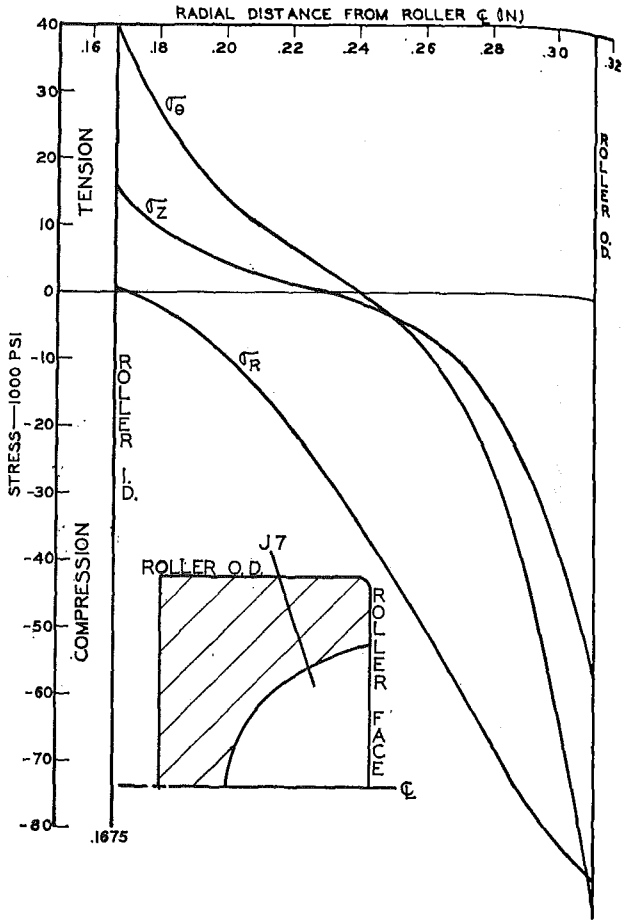


**Fig. 9 Stresses ($\sigma_H$*) across hollow-ended roller thickness (plane J7) in plane of load ($\theta = 0$ deg) from bore to contact surface**

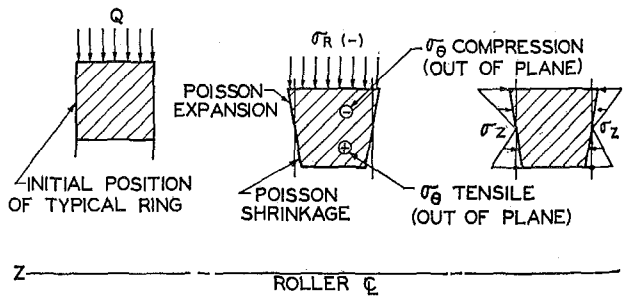


**Fig. 10 Typical ring section of rim with resultant stresses**

To determine the three-dimensional stress state induced by a line load, the rim section is divided into a finite element mesh, Fig. 2, with the stresses computed at the mid-point of each quadrilateral element, with all such midpoints connected to form stress planes $I$ and $J$, Fig. 6. These planes become an important graphic aid in understanding the data evaluation.

The distribution of the principal stresses and resultant maximum shear stresses at a locus just inside the bore surface (viz. along curve A-A) are plotted in Fig. 7. For the purpose of describing the stress orientation, consider an infinitesimal cube with one face in the plane of the bore surface, Fig. 8. Since there can be no shear on the free surface, then the normal to this surface is a principal direction with the respective stress, $\sigma_n$. Next, due to symmetry, there is no shear on the plane defined by $\theta = 0$ deg. This then is a principal direction and $\sigma_\theta$ a principal stress. Finally, since the three principal directions must be mutually orthogonal, the third principal direction is tangent to the bore surface and in the plane $\theta = 0$ deg ($\sigma_t$).

As is conventional the maximum shears occur on four faces of the cube which is rotated about one of the normals, 45 deg from the principal directions. The largest of these maximum shears is determined (considering use of maximum shear theory) by taking the absolute value of the maximum algebraic difference between two stresses. For the example of this paper the greatest maximum shear ($\tau_{t\theta}$) is:

$$\tau_{t\theta} = \frac{\sigma_t - \sigma_\theta}{2} = 24{,}000 \text{ psi}$$

Inspection reveals the location of this shear stress to be at point $P$ (Fig. 7), which is located at $I = 1$, $J = 21$. Similar evaluation of the computer results along the remaining $I$ planes close to the bore surface shows values less than 24,000 psi for this stress. (As a matter of interest, the maximum shear of 24,000 psi is approximately half that found in the preliminary "thin-rimmed" design.) These stresses have a relatively high degree of accuracy, due to the mathematical handling of the loading, as represented by the higher terms of the Fourier series.

Fig. 9 shows the stress distribution along plane $J7$ across the thickness of the rim. The results at the O.D. have not yet been modified to include the effects of the Hertzian contact stress field. The stresses of this stress state will be denoted as $\sigma_H$* or the approximate results for the hollow-ended roller.

To clearly understand the nature and results of the rim section stress analysis which include the exact contact stress, consider a comparison between line-loaded infinite solid and hollow-ended rollers. In the solid roller, the classical Hertzian distribution of stress is obtained [5]. At the surface, the normal and circumferential stresses are compressive and equal to the peak value.

The axial stress is also compressive and equal to $2\nu$ times the peak applied pressure. In the infinite hollow roller the basic stress condition is modified by a gross bending effect (if a simple ring is loaded by opposing concentrated loads, the bending is such as to produce compression on the outer surface under the load). Now the significant shear stress, which may be used as a failure criterion, is described above and is:

$$\tau = \frac{\sigma_R - \sigma_\theta}{2}$$

where, at a small depth inside the O.D. surface, $\sigma_R$ is a larger compressive value than $\sigma_\theta$. The tendency of the hollow roller to make $\sigma_\theta$ more compressive thus makes it more nearly equal to $\sigma_R$, and so reduces the maximum shear.

In the cases of plane strain, the bodies were of infinite length and the loading was uniform. Since the hollow-ended roller is more complex, a numerical approach was used instead of a quantitative mathematical analysis. Consider now the load-carrying mechanism of the hollow-ended roller.

First, consider imaginary cuts at several positions along the axis of the body in the rim section, reducing the structure to a number of rings, each with a different load intensity, Fig. 10. Each of these rings would equilibrate its share of the load, but the radial displacements would be directly proportional to the load, and inversely proportional to the cube of the depth. In general, these would be unequal, and inter-ring compatibility requires transfer of load from each imaginary ring to its neighbors. Since each ring will be in hoop compression under the load, ($\sigma_\theta$ is negative), it will tend to expand in the axial direction and, conversely, shrink at the inside surface. In adjusting these forces in one ring to match those of the next adjacent ring, compressive forces will be required at the outside. All three principal stresses at or near the O.D. (using stress plane $J7$ as an example) should be compressive as illustrated in Fig. 9.

It must be fully appreciated that the use of the "ring" analogy is entirely separated from the "triangular ring elements" used in the finite-element analysis discussion (see previous section).

In order to accurately describe the roller rim stress state in the plane of the actual load (stresses will be at a maximum in this region while decreasing for increasing values of "$\theta$") which includes the Hertzian contact stresses combined with the stress distribution found in the finite-element analysis, an auxiliary finite-element analysis of an infinite solid roller is required to properly combine the two stress states. The results of such an auxiliary analysis are shown in Fig. 11 with the stresses designated $\sigma_S$*, or the approximate results for the solid roller. The finite element stress planes $J$ are the same as used in describing the stress distribution due to the Hertzian contact stress alone, Fig. 12.

The computation of the actual stress state in the hollow-ended roller can now be obtained by assuming the difference between the exact stress ( $\wedge$ ) in the solid ($S$) roller and the exact stress in the hollow ($H$) roller is the same as the difference between the approximate (*) analyses:

$$\hat{\sigma}_H - \hat{\sigma}_S = \sigma_H{}^* - \sigma_S{}^*$$

This is reasonable since the approximate analyses include the basic behavior and do not include the self-equilibrating local effects at the contact area and by St. Venant's principle, these will not be affected by an inner boundary.

The desired stress state:

$$\hat{\sigma}_H = \hat{\sigma}_S + \sigma_H{}^* - \sigma_S{}^* \qquad (1)$$

can now be calculated where $\hat{\sigma}_H$ is an accurate determination of the combined stress state in the hollow-ended roller study, $\hat{\sigma}_S$ is the exact or classical subsurface stress due to Hertzian contact found for a solid roller subjected to the same load distribution (Fig. 3) as the hollow-ended roller, $\sigma_H$* denotes the finite element analysis results for a hollow-ended roller (resulting from the previously described numerical analysis), and $\sigma_S$* denotes the results of an auxiliary finite element analysis on a corresponding solid roller.

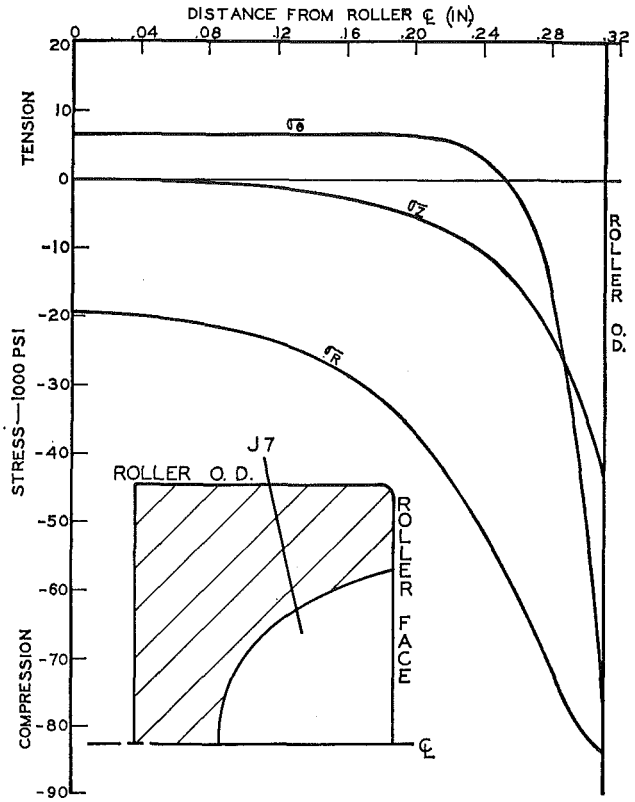


**Fig. 11 Stresses ($\sigma_S$*) resulting from a finite element analysis of a solid roller under a 6550 lb/in. unit load**

A plot of the subsurface stresses, $\hat{\sigma}_S$ due to Hertzian contact along stress plane $J7$ is shown in Fig. 13. The stress planes employed for displaying this stress distribution below the roller surface may be seen in Fig. 12. For practical reasons, the grid is different than that employed in the hollow-ended roller finite element stress analysis although respective $J$ planes have the same surface starting point. However, as the stresses due to Hertzian contact decay rapidly below the O.D. surface and small differences in respective $J$ plane locations (direction) exist in this region little error is involved in the calculation of combined stress due to nonparallelism of the respective $J$ planes.

The $\sigma_H$* stress distribution along plane $J7$ is shown in Fig. 9 as seen above, all three orthogonal principal stresses are compressive at the O.D. with $\sigma_\theta$ and $\sigma_t$ in tension at the bore and $\sigma_R = \sigma_n = 0$ at the bore boundary.

Results of the finite element analysis on a solid roller, $\sigma_S$*, are presented in Fig. 11 using plane $J7$ as an example. The stress plane employed is the same as used for the solid roller subsurface stress distribution presentation, Fig. 12. [The stresses shown in Fig. 11 are valid for a 6550 lb./in. unit load. These stresses may be assigned to $J$ planes whose corresponding unit loading is different, but corrected by the factor: $\frac{J \text{ Plane Unit Load}}{6550}$.]

Using equation (1), plots of the combined principal stresses, $\sigma_R$ and $\sigma_\theta$ for the $\hat{\sigma}_H$ stress state, at various depths across the rim section of the roller are shown in Figs. 14 and 15, respectively. The $\sigma_Z$ distribution was found to be small and is not shown. These three stresses are compressive and have their maximum value in the vicinity of the maximum unit loading.

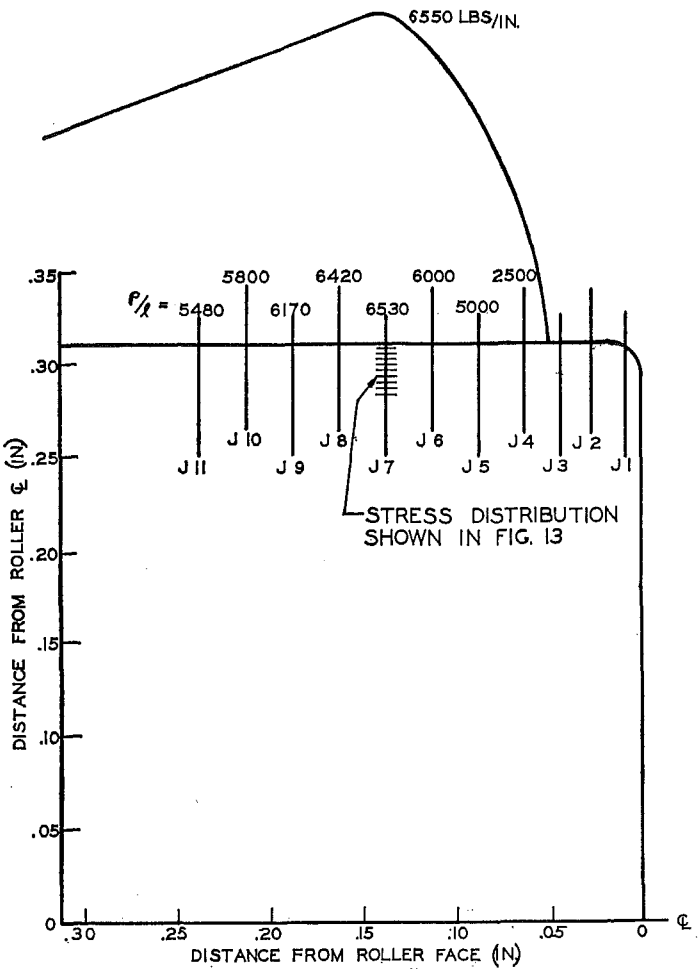


**Fig. 12 Stress planes and load distribution for determination of Hertzian contact stresses ($\hat{\sigma}_S$)-solid roller**

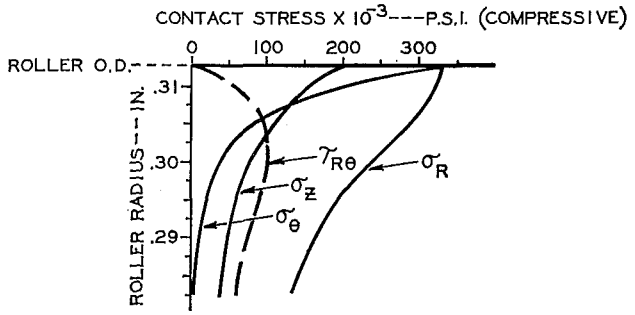


**Fig. 13 Stress state, $\hat{\sigma}_S$, in three orthogonal directions, at various depths below contact surface in load plane ($\theta$ = 0 deg) and along the *J7* stress plane**

The combined shear stresses ($\tau_H$) along plane *J7* is shown in Fig. 16 compared with the maximum subsurface shear stress found in the solid roller ($\tau_S$). Inspection of plots for other *J* stress planes (not shown) shows the maximum combined shear stress for the hollow-ended roller, in all planes, to be lower than the maximum shear stress found in the solid roller.

**NOTE:** The use of stress plane *J7* as the location for evaluating the significant combined stress is the result of preliminary data analysis which showed the highest stresses anywhere on the finite element grid to exist in this area. The Hertzian contact stresses also were of maximum value in the *J7* region.

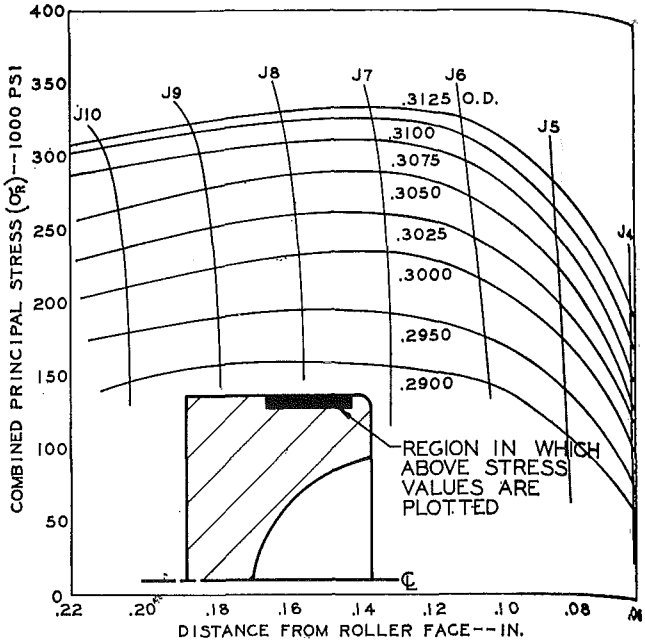


**Fig. 14 Combined principal stress distribution, $\sigma_R$, across the rim at various radii in plane of load ($\theta$ = 0 deg)**

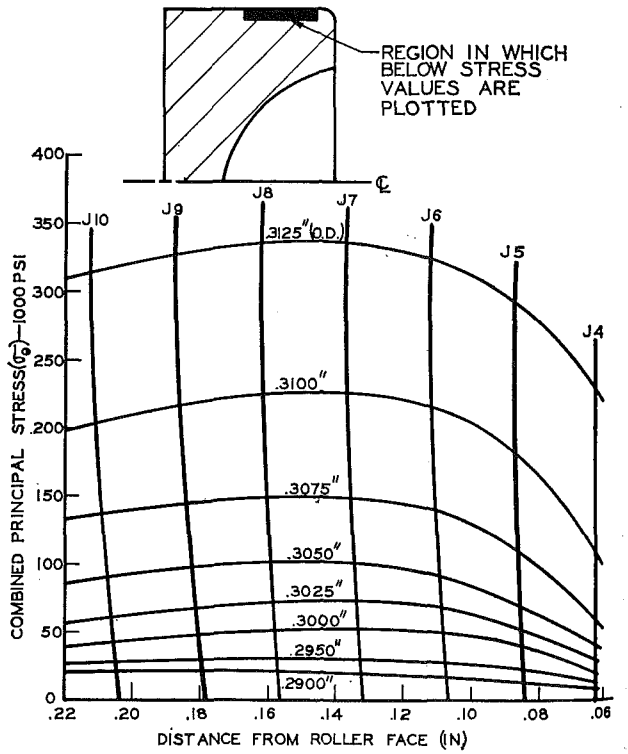


**Fig. 15 Combined principal stress distribution ($\sigma_\theta$) across the rim at various radii in plane of load ($\theta$ = 0 deg)**

## Experimental Evaluation

The life of elements in rolling contact may be determined by the maximum contact stress level which is directly related to the dimensions and shape of contact. Accurate definition and recording of this contact area is possible by employing the footprint technique. In predicting the life of different roller configurations, a measure of the maximum width of the contact area is sufficient, providing roller exterior dimensions are equal. Rollers

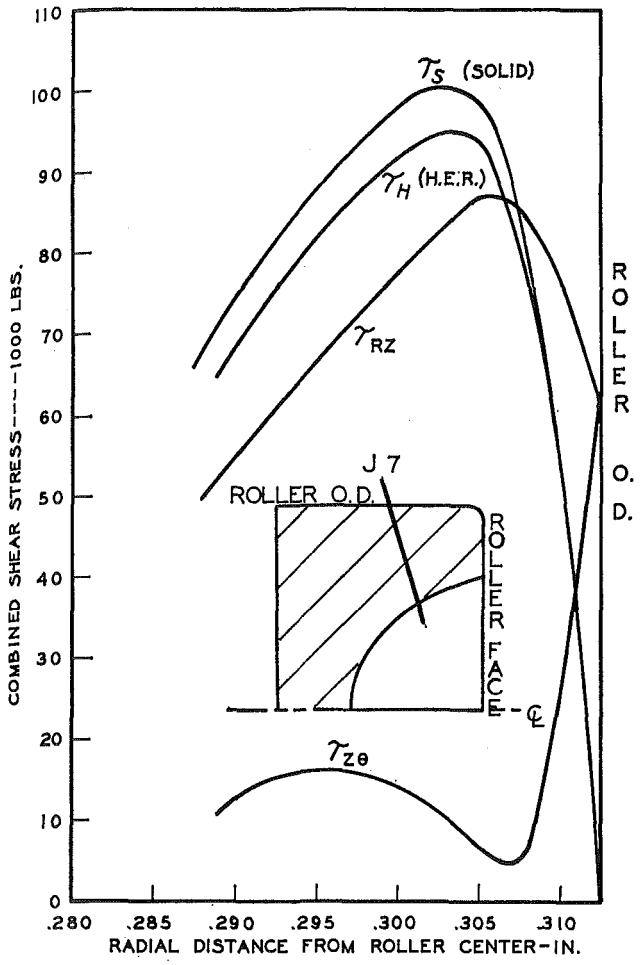


Fig. 16 Combined shear stresses across rim at *J7* in plane of load compared with maximum solid roller shear stress

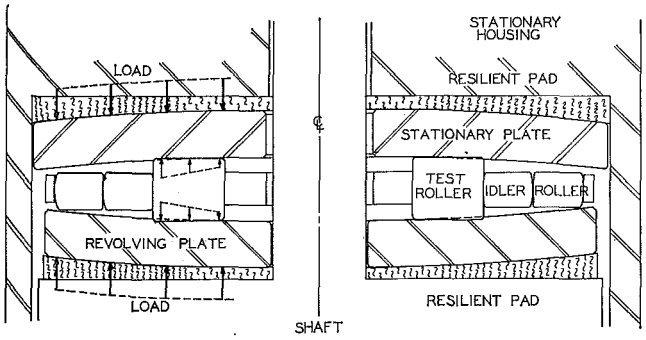


Fig. 17 Fatigue test set-up for hollow-ended and solid rollers

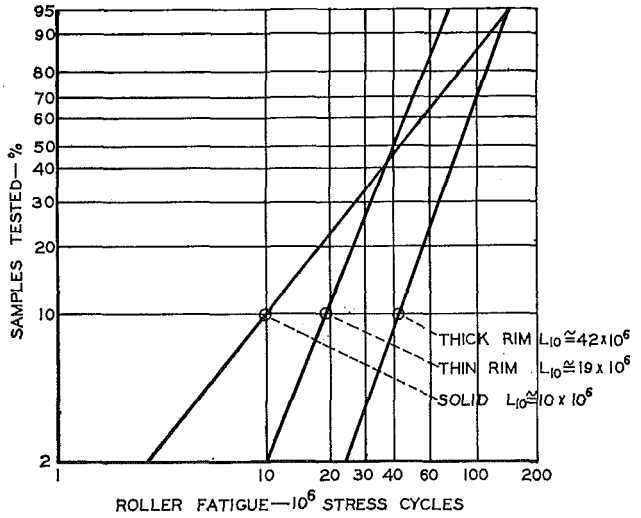


Fig. 18 Weibull distribution (fatigue life statistical plot) for forecast of "B-10" life

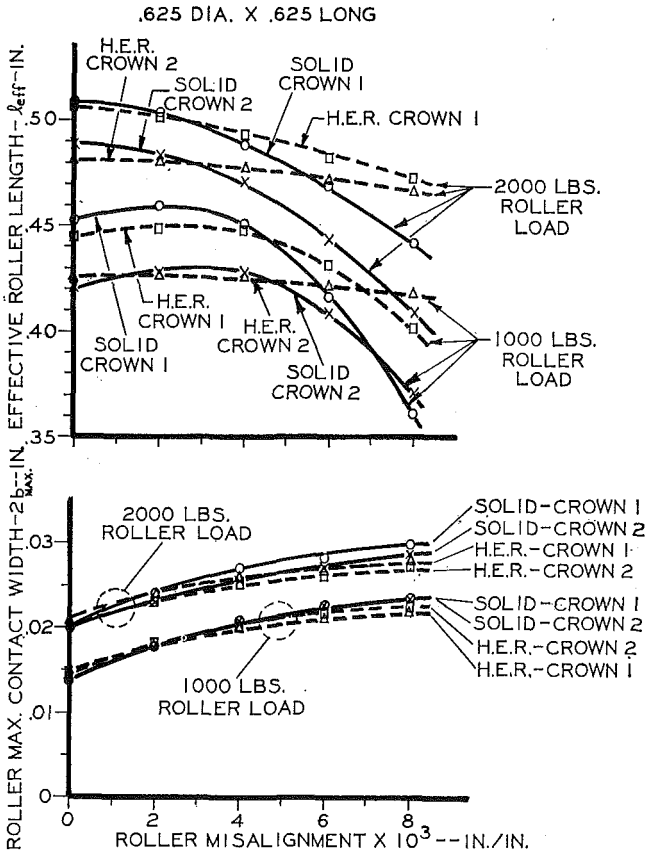


Fig. 19 Effect of misalignment on contact area dimensions

identical with those used in the fatigue test program were employed in this study. Two crown variations were investigated where the hollow-ended rollers had the same crowns as the solid ones. The rollers were pressed on a flat etched plate employing two different loads (selected to insure bulk elastic deformation) and subjected to various misalignment/deflections. The resulting contact areas were measured for length and maximum width with the data presented in Fig. 19. The crowns specified and range of loads and misalignments selected, precluded the development of end-of-contact effects so that all maximum contact widths ($2b$) were found inboard of the end-of-contact. Examination of these curves shows that for significant misalignment, the maximum $2b$ dimension for the hollow-ended roller is less than that for the corresponding solid. This decrease in width is associated with longer contact lengths than those exhibited by the respective solid roller. As the contact width may be associated inversely with rolling element life, the improvement in life due to the flexible rim is clearly demonstrated.

The observations are supported by a more comprehensive analysis. Using the footprint technique, the elastic contact areas resulting from a static 2000 lb test load and 0.008 in./in. misalignment were recorded and displayed graphically in Fig. 20. All three roller variations (thick, thin, solid) had the same crown geometry (but different from the roller crowning used in previous

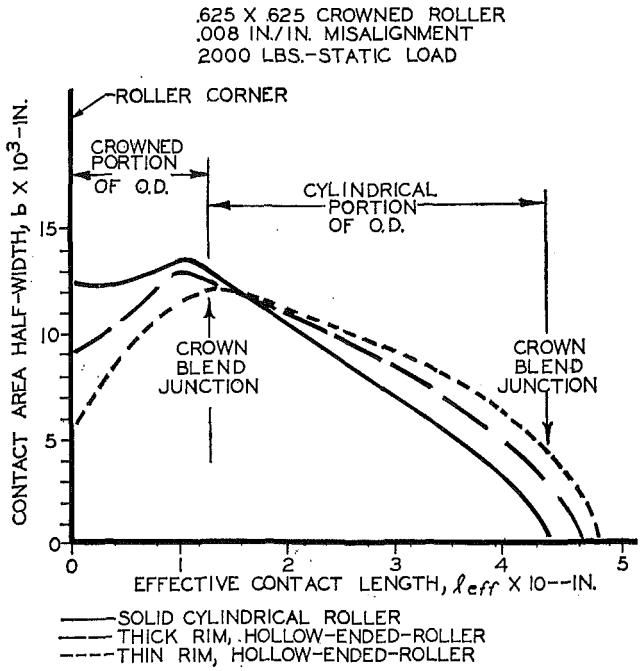


**Fig. 20 Experimentally determined contact areas**

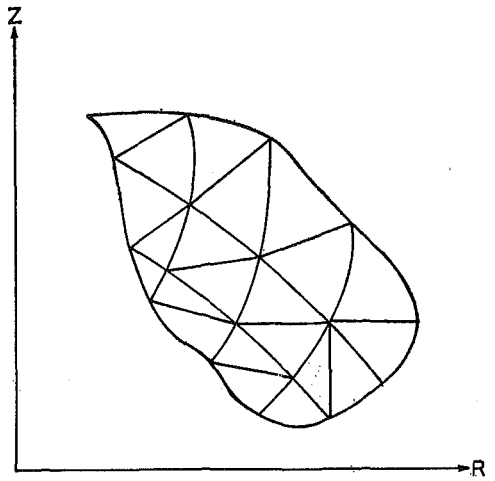


**Fig. 21 Finite element idealization-cylindrical coordinates**

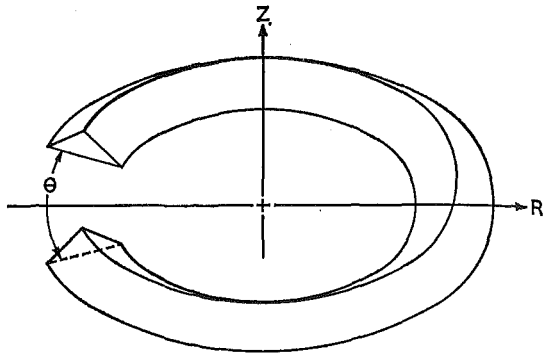


**Fig. 22 Triangular ring element**

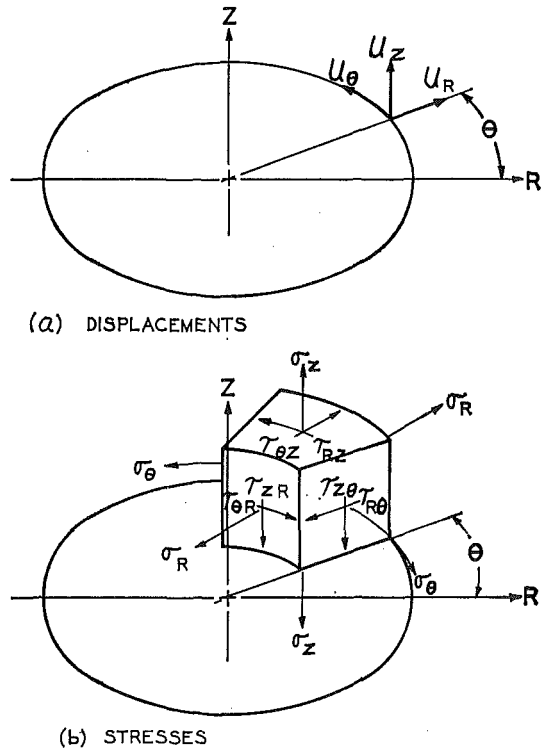


**Fig. 23 Displacements and stresses in an infinitesimal element of roller rim section**

tests). Comparison of these areas show the benefits gained from using a roller with a flexible elastic rim under substantial loading and misalignment conditions. The solid roller displayed no comparative flexibility, had detrimental end-of-contact stresses exceeding those found in the hollow-ended roller, and exhibited the greatest contact width of the three variations represented. The hollow-ended roller's flexible rim distributes the load over a greater contact length with an associated decrease in $2b$ width and end-of-contact stress. It is significant that the aberration in the contact shape due to the crown blend junction is favorably modified by the hollow ends. While it is true that an improved crown on the solid roller could yield a contact area with the end-of-contact phenomena modified to approach that displayed by the hollow-ended roller, this could not be accomplished without increasing the maximum $2b$ dimension and the associated contact stress. Assuming that the significant stress may be used as a basis for life determination in actual applications, and that stress is proportional to contact width, then the improvement to be realized by the hollow-ended roller becomes apparent.

## Fatigue Test Evaluation

A test program was established to determine a bore shape and associated rim thicknesses for the hollow-ended roller that would insure a long-lived and structurally-sound product. Equally important, was the acquisition of supporting data which would independently substantiate the analytical results regarding failure mode and location.

A standard cylindrical roller thrust bearing was employed in all fatigue tests and was modified to run with only one row of rollers, the rest of the pockets filled with undersized spacers, Fig. 17. The stationary plate was hydraulically loaded to 2000 lb load per test roller. As these rollers (located near the plate I.D.) were the only load supporting elements in the system, the plate deflects about them and inherently imposes a misalignment condition on the rolling elements. In this case, as deflection is proportional to applied load and plate thickness the thickness was altered until load distribution, determined by footprint tests, showed the actual misalignment/deflection at the roller to be 0.008 in./in. at the roller compliment pitch diameter. Relatively "thin-rimmed" rollers, Fig. 1 (bore to O.D. ratio of 0.7) were investigated initially and found to crack in the rim section with this

defect rapidly propagating into an O.D. spall. Of a greater detrimental effect, several of the rollers exhibited rim break-up which would, in actual operation, lead to catastropic failure. The deficiency found in the rim section of this "thin-rimmed" series necessitated a bore-rim redesign. A thicker rimmed roller, Fig. 1, was subjected to 15 test runs resulting in 15 cases of failed rollers, where the spalled area was located on the crown at the most heavily loaded end. Rim section break-up was not observed in these tests.

To further support this redesign effort, a number of additional tests were conducted to establish whether rim cracks develop from contact fatigue spalls. Groups of "thick-rimmed" rollers selected from previous fatigue tests (inspection showed no bore cracks or O.D. spalls) were rerun until substantial spalling occurred on the O.D. In an attempt to generate a crack from the spalls, the rollers were run well beyond this stage, or normal useful life, resulting in a much greater spalled area with still no evidence of rim crack initiation.

In a second investigation, a number of unused rollers had flats ground on the most heavily loaded area of the O.D. while others were "Rockwell" indented. These artificially induced surface defects nucleated spalled areas which grew, under continued testing, to include $^2/_3$ of the roller O.D. with no evidence of rim cracks. The results of these studies support the selection of the "thick-rimmed" hollow-ended roller analysed analytically earlier in the paper.

A solid roller test program was conducted to provide a standard for comparison.

Fatigue test results for all three test series are presented in Weibull plot form in Fig. 18, showing the $L_{10}$ life for the "thick-rimmed" hollow-ended roller to be approximately 4 times that of the solid.

## Discussion

Study of various hollow-ended roller configurations permitted selection of the design evaluated in this paper. Bore initiated failures were encountered in fatigue testing of thinner-rimmed hollow-ended rollers, but in all studies the hollow-ended roller proved superior in fatigue life to the solid roller.

Testing in a flat plate thrust bearing with crowned cylindrical rollers contributed to sliding wear causing geometrical changes in the solid roller test elements. These findings were greatly reduced in the bearing assemblies tested with hollow-ended rollers. Since the experimental evaluations were conducted using a medium weight oil, and the surface finish of all these parts was well within specification, this wear phenomenon cannot be considered abnormal. The capabilities of the hollow-ended roller, therefore, must be recognized to include an ability to better utilize lubricant films in reducing wear and possibly improving the load distribution.

The load and misalignment were selected to represent extreme conditions which the hollow-ended roller was expected to endure successfully. Although the test conditions of 0.008 in/in. misalignment may be considered overly severe in some cases, the demonstrated $L_{10}$ life is an appreciable and practical achievement. This deflection was verified in the test rig through footprint tests, the contacts of which were compared to precise footprints on a calibration plate.

Although the emphasis in the overall program was evenly divided between numerical analysis and experimental studies, the authors felt it necessary to describe the stress analysis in detail sufficient to instill some understanding into the more uninformed reader in the field of stress analysis techniques.

The conclusions reached from the stress analysis results are based on a stress state determined from combining local Hertzian contact stresses with those resulting from the deflection of the hollow-ended roller rim due to a line load. The method employed in combining these two stress states is, within the experience of the authors, new, but is substantiated by fatigue test results which show fatigue and wear evidence as would be anticipated from a study of the stress distributions predicted analytically. A rolling-element life comparison between solid and hollow-ended rollers was made considering these results to be the significant stress state.

It also must be appreciated that any element in the roller rim is subjected to a stress reversal as it rotates from the plane of the load to the plane, $\theta = 90$ deg. For the case presented in the paper, the maximum combined shear stress is 95,000 psi in the plane of the load while the maximum shear stress value for the same element, due entirely to rim bending but located 90 deg from the load plane, equals 14,500 psi. The mechanism of this reversal is complicated since the two stress states are entirely dissimilar. Again, as the fatigue tests demonstrates the hollow-ended roller fails in the area predicted by numerical analysis and has a significantly longer life than the respective roller, the authors conclude that the stress reversal is not the controlling life factor. Any discussion, therefore, as to the degree of significance this reversal plays in fatigue life becomes an academic one. If the roller design were changed, however, the influence of stress reversal on life may require additional study.

Summarizing the numerical results shows a maximum bore shear stress of 24,000 psi. The maximum combined shear stress found in the rim is 95,000 psi and is located in the contact region 0.0075 to 0.010 in. below the roller surface. Life may be based on this significant stress value with the failure expected to initiate in this region. In comparison, the peak shear stress calculated for the solid roller is 100,000 psi and located in the same respective region (conventional theory, depth = $0.78b$, indicates that this maximum value should be found 0.00975 in. below surface).

In the numerical analysis, the difference in the significant stress level, considering the same location in the two roller types, is shown to be 5 percent. In the experimental evaluation, however, stress analyses of various footprints, Fig. 20, were conducted resulting in a 7.5 percent significant stress difference between the solid and hollow-ended roller. The reason for disagreement in the two approaches is that the hollow-ended roller load distribution was applied to the solid roller when determining its contact stress distribution (Fig. 13). Employing the same load distribution on each roller type had the advantage of permitting a direct stress comparison with structure flexibility being the only variable. Had the true and more severe load distribution been applied to the solid roller in the analysis, the resultant significant shear stress would have been higher than 100,000 psi bringing the stress differences of the two approaches into better agreement.

Considering the outstanding life improvement shown by the fatigue test (Fig. 18), the difference in stress amplitudes alone does not account for the superior performance of the hollow-ended roller (assuming life varies inversely to a 7th power of the maximum stress). It is the authors' contention that other benefits inherent to the hollow-ended roller configuration are responsible. It is reasoned that improved stress and heat distribution in the end-of-contact area is responsible.

## Conclusions

1 The highest combined subsurface shear stress is found near the surface of the hollow-ended roller, directly under the plane of the load and is less than that of the corresponding shear stress in a similarly loaded solid roller.

2 Fatigue tests and experimental studies support the numerical analysis in respect to failure mode, failure location, and relative life (compared to solid rollers) for the hollow-ended roller.

3 The failure mode in the hollow-ended roller is conventional O.D. spalling, which is normal and predictable, rather than bore initiated.

4 Hollow-ended rollers with bore reliefs in accordance with the "thick-rimmed" configuration operate with bore rim stresses 15 to 25 percent of the maximum combined orthogonal shear stress found near the roller surface.

5 $L_{10}$ lives of hollow-ended rollers under severe misalignment are significantly greater than the lives of solid rollers under the same operating conditions.

## References


1 Harris, T. A., "The Effect of Misalignment on the Life of Cylindrical Roller Bearings," ASME Paper No. 65-Lub-15.

2 Goodelle, R. A., Derner, W. J., and Root, L. E., "A Practical Method For Determining Contact Stresses In Elastically Loaded Line Contacts," *ASLE Transactions*, Vol. 13, 1970, pp. 269–277.

3 Goodelle, R. A., Derner, W. J., and Root, L. E., "Determination of Static Load Distributions From Elastic Contacts in Rolling Element Bearings," presented at ASLE Annual Meeting, Boston, Mass., May 1971.

4 Turner, M. J., et al., "Stiffness and Deflection Analysis of Complex Structures," *Journal of the Aeronautical Sciences*, Vol. 23, No. 9, Sept. 1956.

5 Thomas, H. R., and Hoersch, V. A., "Stresses Due to the Pressure of One Elastic Solid Upon Another," Univ., of Illinois, Engineering Experiment Station, Bulletin No. 212, pp. 26–29, July 1930.

6 Timoshenko, S., and Goodier, J. N., *Theory of Elasticity*, second edition, McGraw-Hill, New York, 1951.

7 Zienkiewicz, C. C., *The Finite Element Method in Structural and Continuum Mechanics*, McGraw-Hill, New York, Revised First Impression, 1958.

8 Sokolnikoff, I. S., *Mathematical Theory of Elasticity*, second edition, McGraw-Hill, New York, 1956.


# APPENDIX

## Finite Element Method

The development of a three-dimensional model from that of a two-dimensional one is relatively straight forward. One of the earlier applications of the latter was the dimensional analysis of planar structures, essentially an approximation of two-dimensional elasticity theory [6]. In the "stiffness" or "displacement" formulation, the body lying in the $X$-$Y$ plane is divided into many finite triangular elements. Within each element, the displacement is assumed to be a linear function of $X$ and $Y$ leading to a constant state of strain (and stress) in the element. Each edge remains straight during deformation. The "stiffness" matrix of such an element may then be calculated by appropriate superposing of all the element stiffness matrices. The elastic properties of the total structure is obtained, and the stresses and displacements corresponding to prescribed load and boundary conditions may then be calculated [7]. These processes are performed by a digital computer program.

Having considered a stress analysis in the $X$-$Y$ plane, extension to axisymmetric loading of bodies of revolution is a natural extension. The $X$ and $Y$ coordinates are placed by cylindrical coordinates $R$ and $Z$, Fig. 21, and the finite element becomes a torus of triangular cross section, i.e., a revolved "triangle" or triangular ring element, Fig. 22. As yet, this is still a two-dimensional problem since the nodes (vertices of triangular elements) are allowed to displace only in the radial ($R$) and axial ($Z$) directions, hence, the displacements are the same for any circumferential coordinate "$\theta$."

This is not adequate to describe the deformation of a roller subjected to axially distributed line loads on opposite sides. However, an assumption is made that the nodes can also move in the circumferential direction and that the amplitude varies sinusoidally with the coordinate "$\theta$." The three displacements, Fig. 23($a$), at each node would be in the form:

$$u_\theta(\theta) = U_{\theta m} \sin m\theta$$

$$u_R(\theta) = U_{Rm} \cos m\theta$$

$$u_Z(\theta) = U_{Zm} \cos m\theta$$

where "$m$" is any integer and the sine or cosine terms are those appropriate to physical symmetry about the plane $\theta = 0$ deg. It can be shown that the solution for the "$m$th" harmonic is independent of each other harmonic, and that the stresses, Fig. 23($b$), have the same behavior.

$$\sigma_\theta, \sigma_R, \sigma_Z, \tau_{RZ} \rightarrow \sigma_m \cos m\theta$$

$$\tau_{\theta R}, \tau_{\theta Z} \rightarrow \sigma_m \sin m\theta$$

The reader unfamiliar with three-dimensional elasticity theory in cylindrical coordinates will find reference [8] helpful.

The various harmonics can be superposed so that solutions are obtainable for any loading condition expressed as a Fourier series in "$\theta$." For example, the pressure at the outside diameter is a variable function of "$\theta$" where:

$$p(\theta) = -\sigma_R(\theta) = \sum_{m=0,\,2,\,4}^{\infty} p_m \cos m\theta \quad \text{(psi)}$$

In the present case of roller loading, a line load at the O.D. varying with $Z$ is considered. Since this load varies in the circumferential coordinate (symmetric about the $\theta = 0$ deg plane) and could be applied at any node, the foregoing procedure permits three-dimensional analysis of arbitrary bodies of revolution under the influence of a symmetric line load in the "$\theta$" coordinate.